https://doi.org/10.5194/egusphere-2026-141
Preprint. Discussion started: 30 January 2026

Automatic Methane Plume Masking Based on Wavelet Transform Image Processing: Application to MethaneAIR and MethaneSAT data

Zhan Zhang[1,2], Maryann Sargent[2], Jack D. Warren[1], Apisada Chulakadabba[3], Marcus Russi[1], Sasha Ayvazov[1], Joshua Benmergui[1,2], Marvin Knapp[1,2], Ethan Kyzivat[2], Christopher C. Miller[1,2,4], Sébastien Roche[1,2,4], Bingkun Luo[4], David J. Miller[2], Maya Nasr[1,2], Kang Sun[5], James P. Williams[1], Katlyn MacKay[1], Mark Omara[1], Luis Guanter[1,6], Ritesh Gautam[1], Jonathan Franklin[2], Xiong Liu[4], and Steven C. Wofsy[2]

[1]Environmental Defense Fund, Washington, D.C., USA
[2]Harvard John A. Paulson School of Engineering and Applied Sciences, Harvard University, Cambridge, MA, USA
[3]School of Computation, Information and Technology, Technical University of Munich, Munich, Germany
[4]Harvard–Smithsonian Center for Astrophysics, Cambridge, MA, USA
[5]Department of Civil, Structural and Environmental Engineering, University at Buffalo, Buffalo, NY, USA
[6]University of Valencia, Valencia, Spain

Correspondence: Zhan Zhang (zhanzhang@g.harvard.edu)

Abstract. Accurate and efficient plume masking is essential for remote sensing-based detection and quantification of methane and other point source emissions, as plume masks are critical not only for quantifying emission rates, but also for visualization and source localization. However, plume masking relies largely on human operation when the retrieved plume concentrations are weak relative to the background, which hinders the automatic plume detection. This study presents an automatic plume masking method based on wavelet transform image processing. Given a methane concentration enhancement image with no prior knowledge of source locations, a 2D discrete wavelet transform is applied to enhance plume signals while suppressing background noise. The binary plume masks are then generated and filtered using criteria such as concentration, plume shape, and wind direction. The method includes tunable parameters to ensure high detection accuracy under varying background and meteorological conditions. This method detected 60% more plumes, mainly with lower fluxes, than a thresholding method from both MethaneAIR and MethaneSAT data, while finding fewer false positives, proving its potential to realize automatic plume detection across platforms at different scales and resolutions. Its high sensitivity to low-volume emissions also enables a lower detection limit and provides a more comprehensive emission rate distribution. Compared to machine learning models, this method is computationally efficient and does not require training data. Although designed for MethaneSAT purposes, this method is broadly applicable for plume detection from concentration imagery on various airborne and spaceborne remote sensing platforms and for numerous atmospheric species.

https://doi.org/10.5194/egusphere-2026-141
Preprint. Discussion started: 30 January 2026

1 Introduction

Detection of point sources of methane has progressed rapidly using remote sensing by airborne and spaceborne imaging spectroscopy in the shortwave infrared (SWIR). Previous studies have demonstrated the methane point source detection capabilities of satellites, including TROPOMI, Sentinel-2, Landsat-8/9, GHGSat, WorldView-3, PRISMA, EnMAP and EMIT (Cusworth et al., 2019; Ehret et al., 2022; Sánchez-García et al., 2022; Thorpe et al., 2023; Guanter et al., 2015). The launches of MethaneSAT and Carbon Mapper in 2024 further advanced methane monitoring efforts by contributing more point source data (Duren et al., 2025; Williams et al., 2025; Guanter et al., 2025a, b). As more instruments and platforms become available, efforts are being directed toward creating open-source methane point source databases for stakeholders, policymakers, and the public. Such efforts necessitate efficient and accurate methane plume detection and quantification methods with low computational cost and minimal human intervention.

A typical methane plume detection and quantification method generally involves two steps: (1) retrieving methane concentrations from radiance data, and (2) detecting point sources and inferring flux rates based on methane concentrations (Jacob et al., 2016, 2022). The second step often requires defining the plume boundary (mask), which is also a crucial input for visualizing plumes and localizing sources (origins). However, the retrieved plume concentrations are not always markedly higher than the background, due to either low plume concentration enhancements or background interference. Consequently, plume masking in practice still depends heavily on human inspection, making the process time- and labor-intensive (Thompson et al., 2015; Guanter et al., 2021). This reliance on manual input creates a bottleneck that increases the cost and time needed for plume detection methods. Furthermore, human inspection may introduce inconsistencies in plume boundary definitions, which in turn increases the uncertainty and may lead to bias in quantification results.

The most common approach to plume masking involves simple thresholding, typically based on concentration values (Duren et al., 2019), percentiles (Sánchez-García et al., 2022), standard deviations (Chulakadabba et al., 2023), or significance tests (Varon et al., 2018). The thresholding is often supplemented with pixel smoothing techniques, such as median filtering, Gaussian filtering, or mask dilation (Varon et al., 2018; Sánchez-García et al., 2022; Chulakadabba et al., 2023). Additional parameters, such as maximum plume length or minimum plume size, are sometimes applied to further reduce artifacts (Duren et al., 2019). However, the effectiveness of thresholding is often hindered by background interference and background noise, which is related to various factors such as upwind emissions, surface features, atmospheric conditions, and instrument sensitivities. This often creates a plume detection dilemma: if we report detections of plumes with relatively low enhancement (i.e., “weak” plumes), we engender a high rate of false detections.

Another type of plume masking approach involves computer vision machine learning (ML) models, which automatically generate plume masks by learning from labeled methane concentration imagery (Jongaramrungruang et al., 2022; Radman et al., 2023; He et al., 2024; Rouet-Leduc and Hulbert, 2024; Růžička et al., 2023). However, these ML models still have several limitations. Firstly, their performance heavily depends on the size and quality of the training dataset. Secondly, published results often report non-negligible rates of false positives (FPs) and false negatives (FNs). In addition, the demand for a large training dataset of ML models results in high computational costs. Furthermore, these models typically need retraining to adapt to

https://doi.org/10.5194/egusphere-2026-141
Preprint. Discussion started: 30 January 2026

different instruments or platforms, though some studies have reported consistent performance across different datasets without retraining (Růžička et al., 2023).

The 2D discrete wavelet transform is an image processing technique commonly used for image denoising and compression. It applies both high-pass and low-pass filters along the two spatial dimensions of an image, decomposing it into low- and high-frequency components. The low-frequency component retains the overall structure, while the high-frequency components capture finer details. In atmospheric science, wavelet transform has been used mainly for decomposing time-series variations of gases and pollutants. In remote sensing applications, wavelet transform has been applied primarily for object detection and removal, such as identifying and eliminating haze and clouds from optical satellite imagery (Schneising et al., 2023). However, studies focusing on methane detection using wavelet transform remain limited. Among the few, Xiao et al. (2020) used wavelet transform to detect singularities in SWIR bands from the Shortwave Airborne Spectrographic Imager (SASI) and identify methane absorption features. Scafutto and De Souza Filho (2018) applied a Difference of Gaussians (DoG) wavelet to reduce noise in methane emissivity imagery derived from midwave infrared (MWIR) airborne hyperspectral data. However, previous studies have yet applied wavelet transform specifically for plume masking in SWIR-retrieved methane concentration imagery.

In this study, we introduce an automated methane plume masking method based on wavelet transform. First, noise signals are extracted and subtracted from the input image to produce an enhanced image with enhanced plume signals. Binary plume masks are then generated from this processed image using a combination of thresholding and a connected component algorithm. Subsequently, multiple mask filtering techniques are applied to remove false detections. We evaluated the model using airborne methane concentration data from MethaneAIR campaigns in 2021-2023, as well as MethaneSAT satellite concentration data in 2024-2025. Our method requires less human inspection than simple thresholding by reducing background noise. It also has a lower computational cost than ML models as it is an unsupervised classification with no training process needed. Although designed for MethaneSAT purposes, the model is broadly applicable for plume detection from concentration imagery across various platforms and species.

2 Data and Methods

2.1 Data

2.1.1 MethaneSAT

MethaneSAT (operational March 2024 – June 2025) occupied a unique position in the world of methane satellites by providing a comprehensive global picture of oil and gas methane emissions at high spatial resolution. It characterized methane from both dispersed area sources and discrete point sources in more than 80% of global oil and gas production. With its high spectral resolution (0.24 nm) and spectral sampling (0.08 nm), large swath width (200 km), and fine spatial sampling (110×400 m^2), MethaneSAT provided clear signals of strong point source emissions (Guanter et al., 2025a). In this study, our input data is the full-scene level-3 (L3) methane concentration map (pixel size: 45×45 m^2) produced by the CO_2 proxy retrieval method,

https://doi.org/10.5194/egusphere-2026-141
Preprint. Discussion started: 30 January 2026

which typically achieves 25-55 ppb precision for a single pixel (Chan Miller et al., 2024). Cloud-contaminated and low-quality soundings were masked during upstream pre-processing.

2.1.2 MethaneAIR

MethaneAIR is an airborne image spectrometer developed as a demonstrator of the MethaneSAT satellite. With a 12 km flying altitude, a 4.5 km observing swath, and fine spatial resolution (5×25 m^2), MethaneAIR is also designed to provide emissions information from both dispersed area sources and discrete point sources. Previous studies have validated MethaneAIR's performance on point source emissions using different retrieval methods and plume quantification methods (Chan Miller et al., 2024; Guanter et al., 2025b; Chulakadabba et al., 2023; Warren et al., 2025). Similar with what we did with MethaneSAT data, we also took the full-scene L3 methane concentration map (pixel size: 10×10 m^2) produced by the CO_2 proxy retrieval as input.

2.2 Methods

The key step is to generate a denoised version of the column-averaged dry-air mole fraction of methane (XCH_4) image by applying the wavelet transform to filter out noise and enhance plume signals. Using the denoised image, we then create binary plume masks, determine source locations, and remove false detections. The input XCH_4 image is the full scene of the L3 data from a MethaneAIR flight or a MethaneSAT collection. The detailed steps are as follows.

2.2.1 Wavelet denoising

We adapt an approach used in medical image processing, providing its first implementation in atmospheric studies (Hüpfel et al., 2021). Our method begins with a pre-processing step, which converts strong signals to low frequencies so that it is easier to separate them from high-frequency noise. In this step, all pixels above a defined threshold are assigned a uniform value. For MethaneAIR, the threshold is uniform across the scene, determined as the mean value of the whole image scene plus a scaling factor (value: 2) times the standard deviation of the whole scene; and for MethaneSAT, the threshold is adjusted in varying local background, defined as the mean value of a localized (4.5×4.5 km^2) area of the image plus a scaling factor (value: 1.75) times the standard deviation of this local area. Then pixels above this threshold are set to the maximum value of the entire image (Fig 1(a)-(b)). The sensitivity analysis of the scaling factors and the local background size are discussed in the SI Section 1.1. These parameters were chosen to maximize plume detections while minimizing FPs, and can be tuned for different observing platforms. The resulting image is referred to as the "input image" (Fig 1(b)).

After pre-processing, a multilevel 2D discrete wavelet transform is applied to the input image to generate approximation and detail coefficients. The wavelet filter is applied in both horizontal and vertical directions on an image of size $m \times n$, producing four coefficient matrices of size $\frac{m}{2} \times \frac{n}{2}$ (cA_1, cH_1, cV_1, cD_1), where cA_1 represents the approximation and (cH_1, cV_1, cD_1) represent the details. This decomposition process is repeated recursively on the approximation coefficients, creating additional levels of details, each level capturing finer aspects of the image. The resulting coefficient list includes the approximation

https://doi.org/10.5194/egusphere-2026-141
Preprint. Discussion started: 30 January 2026

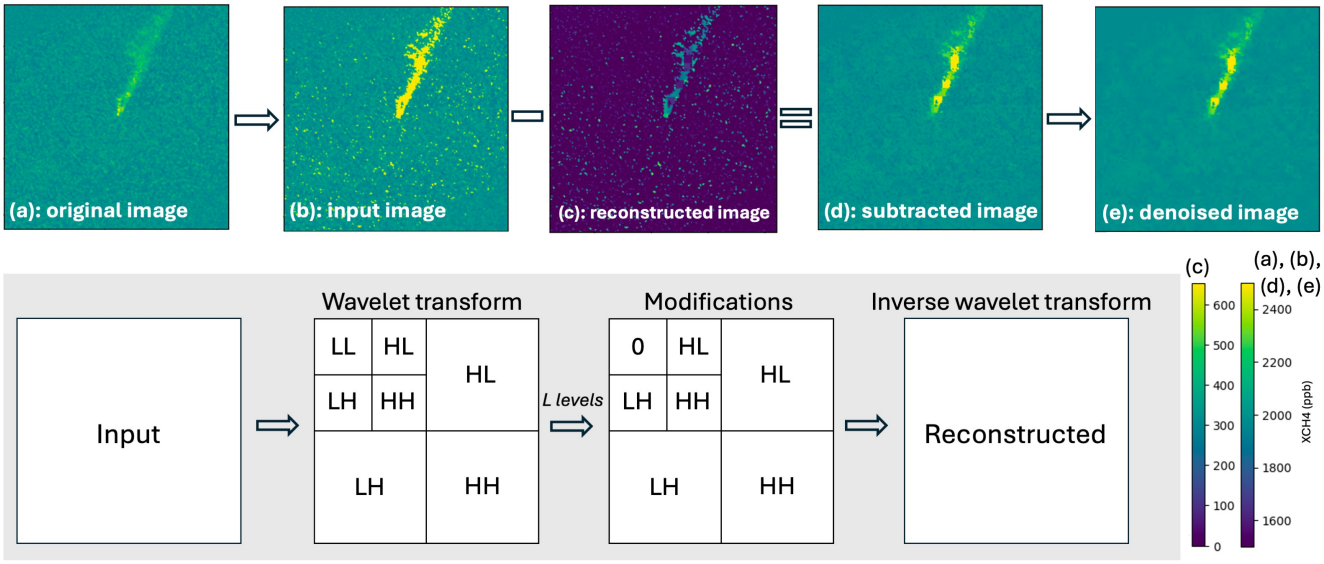

Figure 1. Wavelet denoising workflow. (a): an original image example; (b): output of pre-processing; (c): output of wavelet transform and inverse wavelet transform with low frequencies removed; (d): output after subtracting (c) from (b); (e): output of applying soft thresholding wavelet denoising to (d).

coefficients at the L-th level of decomposition and tuples of detail coefficients in descending order of the decomposition level (Eq 1). We used the Haar wavelet in this step for its simplicity and computational efficiency (Hüpfel et al., 2021).

$$Coefficients = (cA_L, (cH_L, cV_L, cD_L), ..., (cH_2, cV_2, cD_2), (cH_1, cV_1, cD_1)), L = \log_2(min(m,n))/2 \quad (1)$$

After decomposition, a common denoising approach involves setting the detail coefficients to zero and then performing an inverse 2D discrete wavelet transform (Hüpfel et al., 2021). This reconstructs an image of the same size as the input, with the approximation retained and high-frequency details removed. However, this approach causes a loss of detailed plume structure, which is essential for plume visualization. To address this, we followed Hüpfel et al. (2021) and set the approximation coefficients (cA_L) to zero and performed the inverse wavelet transform, building an image that retains only high-frequency components (Fig 1(c)). We then subtract this high-frequency image from the input image, so that the resulting image greatly minimizes noise and enhances plume signals while maintaining a detailed plume structure (Fig 1(d)).

In this process, the decomposition level L is a key parameter. If L is set too low, it may fail to capture sufficient noise signals, while a level that is too high risks capturing plume signals along with noise. To balance these effects, we set L at half of its maximum possible value (Eq 1).

Finally, we apply soft thresholding wavelet denoising to the processed image for further denoising. This reduces small noise-associated coefficients while retaining larger coefficients likely to represent meaningful features. Once completed, the wavelet coefficients are transformed back to the original domain, producing the final denoised image (Fig 1(e)). Note that the

https://doi.org/10.5194/egusphere-2026-141
Preprint. Discussion started: 30 January 2026

pixel values in the denoised image no longer retain their physical meaning and are therefore unsuitable for flux quantification. Instead, the denoised image is used only for plume masking.

2.2.2 Mask generation

Based on the denoised image, the plume masks are generated in the following two steps. First, pixels above a threshold value are preserved, where the threshold is defined as the local mean plus a scaling factor (value: 1.5 for MethaneAIR, 1.75 for MethaneSAT) times the local standard deviation (again, the sensitivity tests of these parameters are discussed in the SI Section 1.1). Note that the threshold is determined on the basis of the local background to better fit the varying regional background concentrations. Second, XCH_4 clumps are identified from these preserved pixels using the 8-connectivity connected component algorithm, which groups adjacent pixels into connected components based on their 8 neighboring pixels. Clumps are then preserved if they exceed a size threshold (100 pixels for MethaneAIR, 500 for MethaneSAT; see their sensitivity analysis in SI Section 1.1). Although binary masks are generated from the denoised image, they are applied to the original concentration image for further quantification to conserve mass.

2.2.3 Mask filtering

Given a set of plume masks, we further filter out false masks by applying specific criteria based on concentrations, plume shapes, and wind direction.

Concentration filtering. The concentration filter aims to remove false masks by finding a high concentration "hotspot", a smaller XCH_4 clump with elevated pixel values within the mask. The rationale is that a plume typically features a central hotspot with higher enhancements near the source, diffusing into lower enhancements along the wind direction as the plume spreads out.

The hotspot is defined by a pixel value threshold and a size threshold (10 pixels for MethaneAIR, 20 for MethaneSAT, see their sensitivity analysis in the SI Section 1.1). The pixel value threshold is adjustable to the regional background concentration variations resulting from different surface types, weather conditions, etc. We define a hotspot filtering criterion named the hotspot ratio, which is the ratio of the hotspots pixel count to the total pixel count of the mask. Masks with a low hotspot ratio are discarded, while those with a high hotspot ratio are accepted without further filtering. Masks with a hotspot ratio in between are further evaluated by the latter filters.

Shape filtering. Plumes can take various shapes affected by factors such as flux rate, duration, wind speed and direction, and instrument detection limits. A well-defined plume may appear long and narrow under high winds or in an ellipse or circular shape under low winds. Sometimes the plume may be split into multiple clumps by local eddies, alternating between regions of higher and lower enhancements, resembling several detached bubble-shaped plumes (Fig S3). Therefore, in the shape filtering process, we do not restrict our criteria to "standard" plume shapes. Instead, we discard masks with unusual shapes that are clearly not plume-like.

One specific shape to eliminate is the "spider" shape, which consists of multiple branches extending and curling from the center of the mask (Fig S1). To quantify the degree of curl in such shapes, we introduce the concept of "fiber length", defined

https://doi.org/10.5194/egusphere-2026-141
Preprint. Discussion started: 30 January 2026

as the length of the longest path along the mask's skeleton (Fig S1). For a mask in spider shape, the curling branches lead to a significantly longer fiber length compared to its major axis length (the longest straight line that lies between two boundary points). Based on this observation, we defined a shape filtering criterion by calculating the ratio of fiber length to major axis length, discarding masks with excessively high ratios. The specific parameters used are provided in the SI Table S6 and Table S14.

Wind direction filtering. Plumes typically extend along the wind direction, which provides a useful criterion to filter out false masks. To achieve this, meteorological wind data needs to be collected, and the plume origin needs to be identified. In this study, we use High-Resolution Rapid Refresh (HRRR) wind data for U.S. scenes and Global Forecast System (GFS) wind data for all other international scenes. Based on the wind data, the plume origin is determined as the farthest upwind end of the mask.

For scenes captured over multiple hours, which is typically the case in airborne campaigns, we obtain a range of hourly wind angles from meteorological datasets for the plume origin. Since meteorological data are often coarse both spatially and temporally, we add an angular buffer (55°) to the upper and lower bounds of the wind angle range (its sensitivity is discussed in SI Table S5 and Table S13). For scenes captured at a specific moment, as is often the case with satellite snapshots, we collect a single wind angle and similarly apply angular buffers to get a wind angle range. Finally, we calculate the plume-derived wind angle based on the plume origin and its major axis. Only the plume whose derived wind angle falls within the meteorological wind angle range is preserved. Note that plumes that passed hotspot filtering are not subjected to wind direction filtering, so that high-volume plumes are not removed even if the meteorological product's wind direction is wrong.

2.2.4 Flux rate quantification

In this study, the divergence integral (DI) growing-box method is used to quantify the flux rate of each plume, in which Gauss's theorem is used to estimate the flux divergence fields through a series of closed surfaces enclosing the source. The DI growing-box method has been introduced in Chulakadabba et al. (2023), and here we briefly outline the key steps of implementation. Given a plume origin and the length of the XCH_4 mask, we use the unfiltered XCH_4 map and draw a series of rectangles ("growing boxes") surrounding the plume origin, with a distance from the origin to the downwind edge of each rectangle ranging from approximately 100 m to the full plume length. Consequently, each successive rectangle is larger than the previous one and completely contains it. The incremental distance between rectangles is one pixel width in each direction, except for the upwind side, where the increment is a quarter of the pixel width. Then based on the measured XCH_4 along each rectangle, we calculate the surface flux divergence integral (kg/h). The resulting fluxes are then aggregated into a final flux by taking the average over all rectangles that cross the plume. Wind speed from the meteorological product was used for this calculation, and for sufficiently oblong plumes (eccentricity > 0.87), the wind direction was rotated to match the angle of the the major axis of the observed plume.

https://doi.org/10.5194/egusphere-2026-141
Preprint. Discussion started: 30 January 2026

2.2.5 Validation

Although the proposed wavelet-based plume detection method operates without manual input, all plume detections presented in the Results section were manually validated. This validation included attribution to emitting infrastructure through review of high-resolution satellite imagery by independent analysts, as well as cross-checking against plume detections identified by other peer methods (Warren et al., 2025).

3 Results

3.1 MethaneAIR results

MethaneAIR campaigns conducted between 2021 and 2023 covered all major oil and gas regions in the United States, accounting for 80% of the nation's onshore oil and gas production. Warren et al. (2025) provided an in-depth analysis of point source attributions for over 400 methane plumes found across all MethaneAIR flights. To identify plumes, they used a gridded application of the DI thresholding method (separate from the DI growing-box method) where the flux divergence was calculated for 600×600 m^2 squares tiled across each scene. Thresholding and clumping were used to find locations with both elevated flux pixels and elevated XCH_4 concentrations. Plumes were then quantified with the same DI growing-box method used in this study. Their analysis found a total flux rate of 360 t/h (95% CI: 285-445 t/h) from point sources across 13 major US oil and gas basins from flights in 2023.

We applied the wavelet-based plume detection method to 46 flights where 375 plumes were previously found by Warren et al. (2025). The wavelet method identified 551 plumes, among which 262 were not previously detected. We used the same DI growing-box method as Warren et al. (2025) to quantify flux rates, allowing for direct quantitative comparison. Since the plume masks created by the two detection methods can be different, this procedure may introduce biases to flux estimates. However, we observed a small flux difference (within one-sigma) for most of the plumes found by both methods, suggesting that the biases are negligible.

We observed that most of the plumes detected only by the wavelet method were in lower flux ranges, and the most frequently observed flux rates decreased from 600-1000 kg/h in Warren et al. (2025) to 200-600 kg/h when added with the additional plumes found by the wavelet method (Fig 2). This indicates that the wavelet method has a higher sensitivity to "weak" plume signals, thus achieves a lower detection limit in MethaneAIR data. We present two MethaneAIR plume examples to demonstrate how the wavelet method effectively captures plumes with lower flux rates (Fig 3). A full list of the 262 additional plumes can be found in the SI.

The wavelet method found 181 FPs and 86 FNs compared to the DI thresholding method, with significant variations between different flights (FPs were determined by manual inspection, and FNs were determined with reference to DI's true detections). In contrast, the DI thresholding method yielded 919 FPs and 262 FNs compared to the wavelet method. Background interference plays an important role in the variability between different flights, as the "cleanliness" of the background differs greatly across these flights. This variation is usually related to the amount of nearby emissions, the characteristics of the basin surface,

https://doi.org/10.5194/egusphere-2026-141
Preprint. Discussion started: 30 January 2026

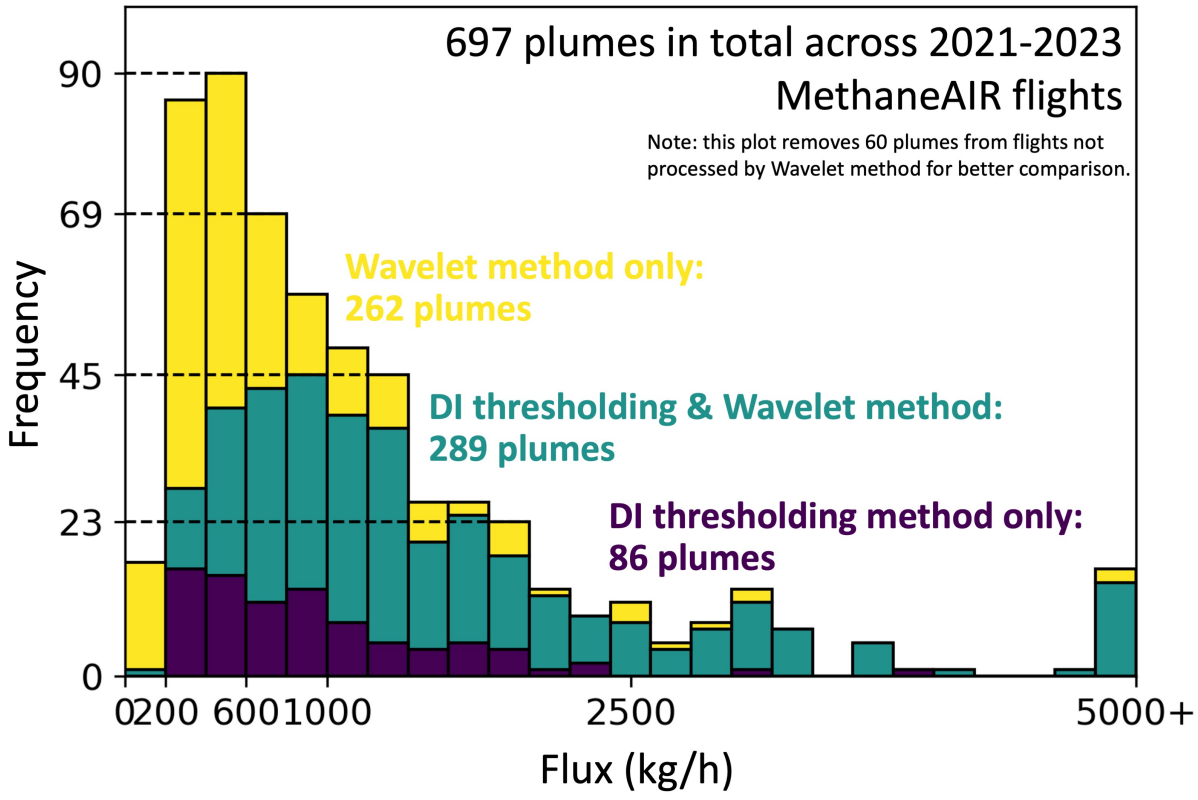

Figure 2. MethaneAIR plumes stacked histogram. Most of the plumes found only by the wavelet method (yellow) lie in lower flux ranges. Most frequently observed flux rates moved from 600-1000 kg/h to 200-600 kg/h when added with additional plumes found by the wavelet method.

the existence of clouds, and the instrument differences between campaigns. This suggests that background interference remains a major challenge in plume detection; although the wavelet method substantially reduces noise, it does not eliminate it. Future work on improving concentration thresholding, masking clouds and cloud edges, and identifying albedo artifacts can reduce background interference.

Diffuse enhancements are another important source of FPs. We define these as XCH_4 clumps that arise from sources well upwind, where the enhancement has spread out and lacks the "hotspot" typically found near the source of the plume. Diffuse enhancements can be caused by intermittent sources that stopped emitting, where the plume is observed a significant distance downwind from the source (Fig S2). They can also arise from large plumes that are dissected by eddies into multiple detached clumps as the enhancement spreads downwind (Fig S3). This can cause the wavelet (as well as DI thresholding) algorithms to produce multiple masks representing parts of the same plume. This is particularly challenging for MethaneSAT and MethaneAIR as a result of their high sensitivity, with clear signals observed well downwind that would not be detected by

https://doi.org/10.5194/egusphere-2026-141
Preprint. Discussion started: 30 January 2026

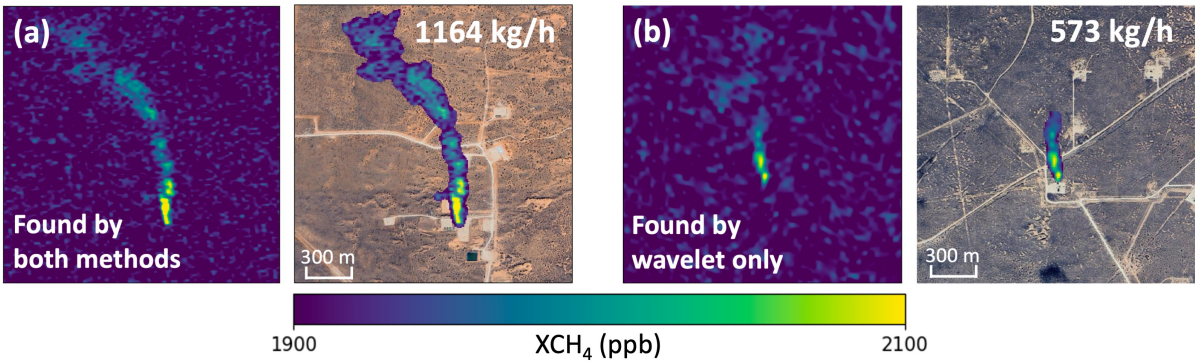

Figure 3. MethaneAIR plume examples (background © Google Maps 2023). Compared to the DI thresholding method, the wavelet method efficiently captured more low-flux plumes like (b).

many other platforms. Since our method is primarily signal-based, it sometimes struggles to differentiate between concentrated plumes and diffuse emissions. Although many diffuse emissions were successfully filtered out by concentration filtering and mask size thresholding, some were still identified as plumes. Future work could potentially address this by analyzing the spatial distribution of enhancements and plume morphology.

Nearby sources also pose a challenge when plumes merge and multiple plumes are grouped within the same mask (Fig S4). In this case, we tend to treat the combined plume as a single source and quantify the total emissions from both sources together. Addressing this issue may involve analyzing the hotspot locations, the distance between masks, and the wind direction. Until our method is refined to better handle these complexities, some level of manual inspection will still be required to achieve a zero-FP dataset.

3.2 MethaneSAT results

With its high spectral resolution (0.24 nm) and large swath width (200 km), MethaneSAT provided clear signals of emissions not only near the source but also a significant distance downwind. However, these capabilities also introduce new challenges for plume detection, as not all emissions can be directly attributed to specific point sources or reliably quantified. Its coarser spatial resolution (110×400 m^2) relative to point source imagers also makes it more difficult to differentiate spatially close point sources.

We applied both the wavelet and the DI thresholding methods to 23 MethaneSAT scenes in 2024-2025 and compared results (Fig 4). The wavelet method achieved an equal or higher number of true detections and a lower number of FPs in most scenes (again, FPs were determined by manual inspection). In some cases, the improvement of true detections (collection 2) and the reduction of FPs (collection 6) is significant. This is consistent with what we observed in MethaneAIR data, indicating that the higher sensitivity of this method to "weak" plume signals generally holds true across different platforms. Fig 5 offers a similar quantification comparison to what we did with MethaneAIR, where we again observed a higher contribution of the wavelet method to low-volume emissions. The most frequently observed flux rates lay in the range of 2-3 t/h, although we probably

https://doi.org/10.5194/egusphere-2026-141
Preprint. Discussion started: 30 January 2026

missed data in the range 3-7 t/h due to the small sample size. More detailed analysis with a larger dataset under different surface features and wind conditions will be needed to determine the detection limit.

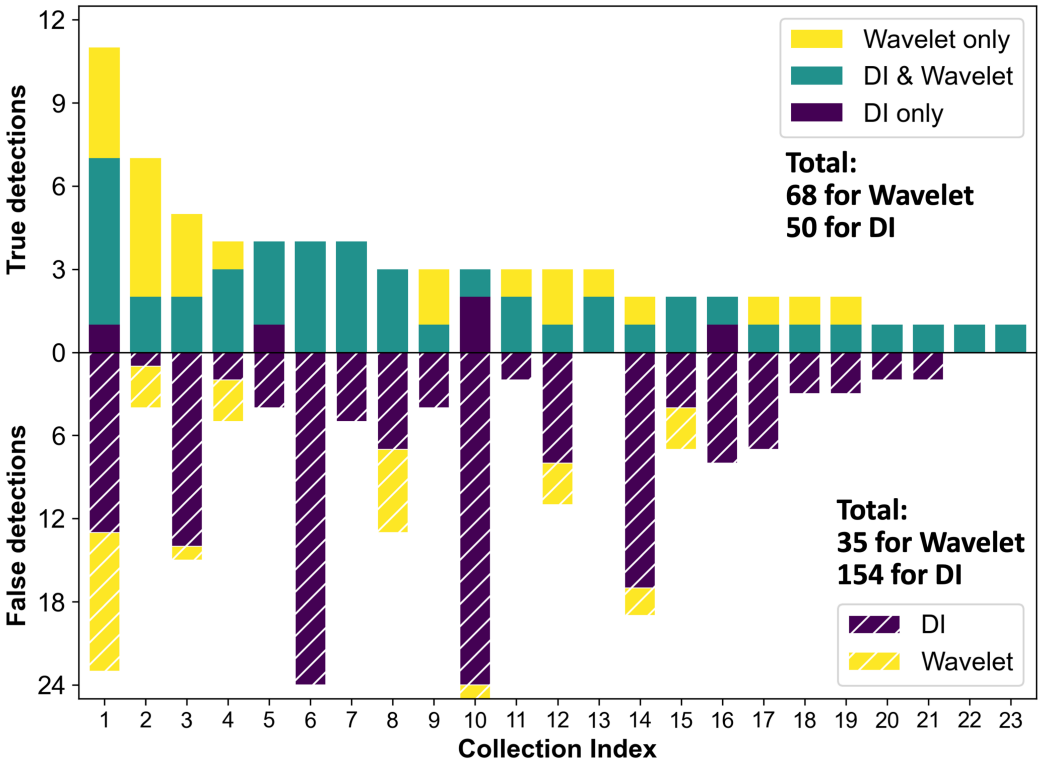

Figure 4. Detection performance of the wavelet and DI thresholding methods on MethaneSAT scenes. Compared to the DI thresholding method, the wavelet method generally found a higher number of true detections and a lower number of false detections.

Fig 6 presents a MethaneSAT XCH_4 image with plumes segmented using the wavelet and DI thresholding methods. Compared with MethaneAIR, MethaneSAT captured significantly longer downwind plume tails, portions of which extended beyond the wavelet mask boundaries. We did not expand the plume masks farther downwind, as doing so would require lowering the plume-detection thresholds, which increases the probability of more false detections. In addition, restricting the masks to the plume segment within 5–10 km of the source generally produces more accurate flux estimates, because expanding the masks farther downwind increases the chance of including nearby sources in the DI growing boxes, thereby biasing flux calculations. Averaging the fluxes from growing boxes spanning 5-10 km still provides sufficient data for a robust average flux estimate.

We generally found more false detections for MethaneSAT than MethaneAIR using both the wavelet and DI thresholding methods, primarily because the high sensitivity of MethaneSAT led to more frequently observed diffuse plumes (long plume tails disected into separate clumps). Such emissions lack high-concentration hotspots that indicate clear source locations. This suggests a need to improve our concentration filtering technique for MethaneSAT observations to minimize the need

https://doi.org/10.5194/egusphere-2026-141
Preprint. Discussion started: 30 January 2026

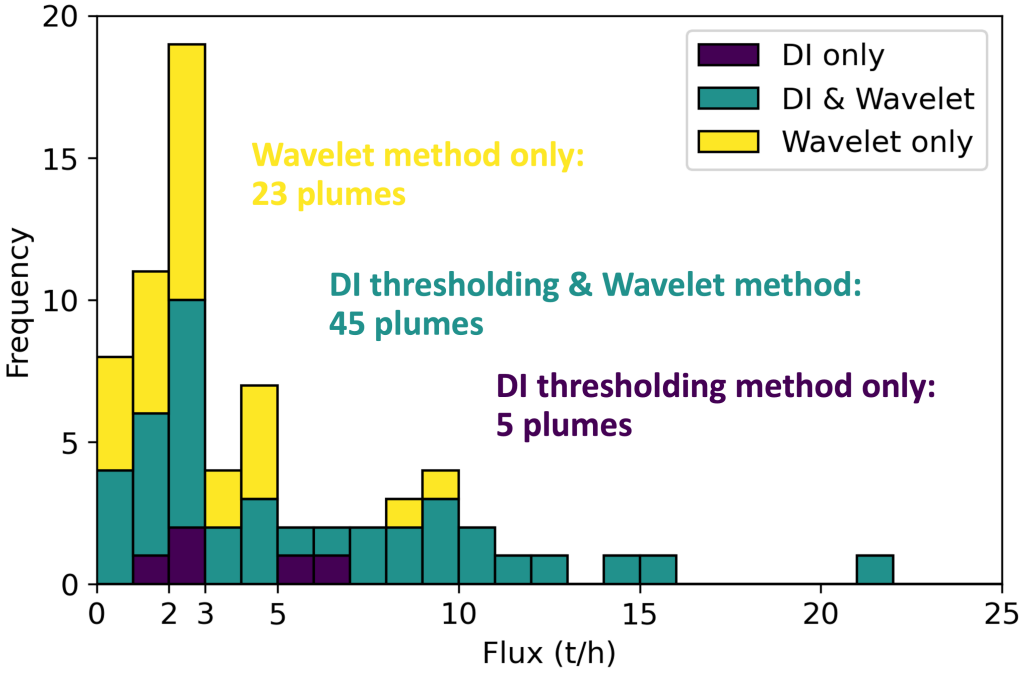

Figure 5. Plumes stacked histogram across 23 MethaneSAT scenes. Similar with MethaneAIR, most of the plumes found only by the wavelet method (yellow) are in lower flux ranges.

for human inspection. Another challenge that occurred more often on MethaneSAT is the presence of overlapping plumes. Because MethaneSAT captured longer plume tails, the downwind ends of the plumes in proximity are more likely to overlap. This increased the difficulty of quantification as it required manual adjustment of the plume length. Potential ways to address this problem are to explore plume segmentation techniques.

Future plume detection improvements can be explored in two directions in parallel. Currently, the wavelet method is applied to the whole scene with no prior information of point source locations. Looking ahead, we plan to further improve its sensitivity to plume signals by applying targeted wavelet denoising to subregions where plumes have been identified in previous top-down surveys, or where known oil and gas infrastructure exists. Additionally, artifact identifiers targeting specific artifact types can be developed and integrated into the plume detection models. Such tools can reduce the number of false detections, and at the same time allow lower plume-finding thresholds to maximize the number of true detections.

4 Conclusions

In this study, we propose a new automated methane plume masking method that uses atmospheric methane concentration data with no prior knowledge of source locations, to find plumes, determine plume origins, and create binary masks. This

https://doi.org/10.5194/egusphere-2026-141
Preprint. Discussion started: 30 January 2026

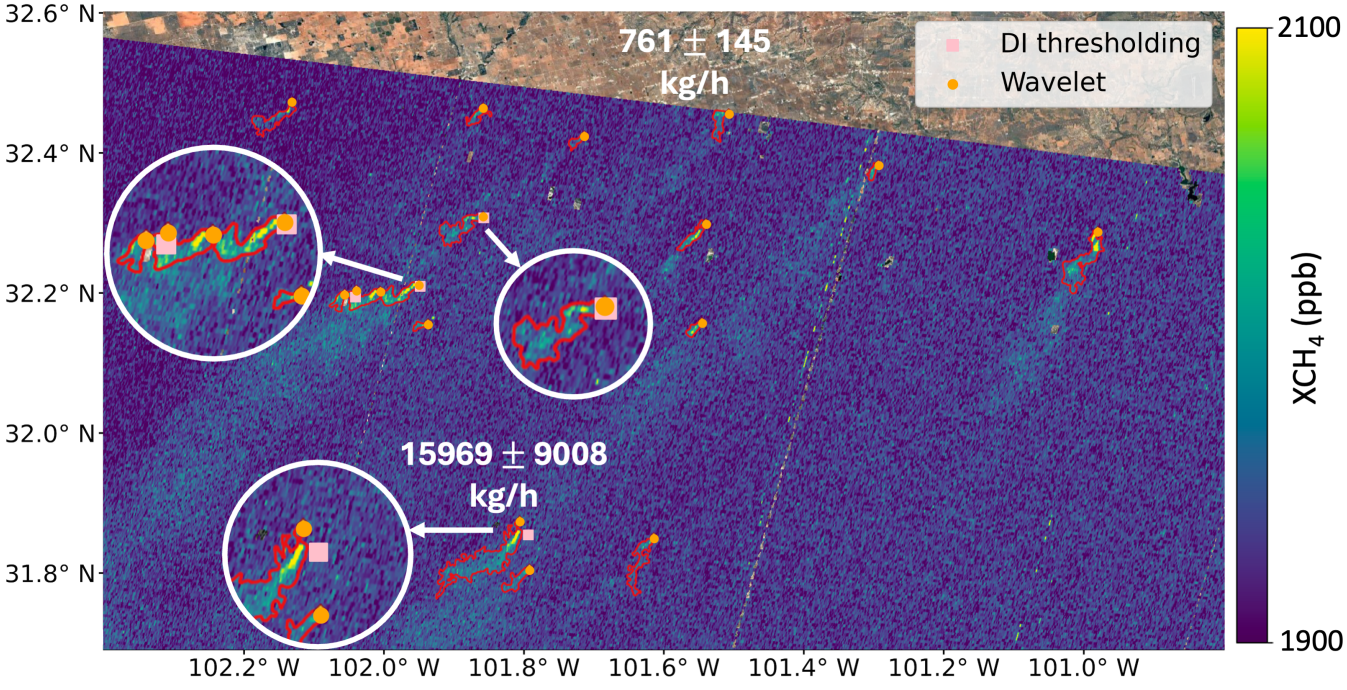

Figure 6. MethaneSAT plume examples (background © Google Maps 2023). Both the DI thresholding method and the wavelet method found 4 plumes (the zoomed-in view), and the wavelet method found additional 13 plumes. Flux rates range between 1-10 t/h, with the lowest and highest marked adjacent to the plume sources.

method uses a 2D discrete wavelet transform, a technique typically used in image processing, to enhance plume signals and reduce background noise in XCH_4 imagery. It significantly improves the effectiveness of thresholding by more precise separation between plume and background signals. We demonstrate the performance of this method using both airborne data from MethaneAIR and spaceborne data from MethaneSAT. Across these platforms,the wavelet method consistently performed well, with particularly higher sensitivity to weak plume signals that are more often missed by conventional techniques.

Certain challenges still remain. Diffuse emissions with elevated concentrations but no clear hotspots can be difficult to differentiate from plumes. Moreover, we occasionally observed the method not capturing the full shape of a plume or capturing multiple plumes into a single mask. Addressing these issues will require additional post-processing steps targeted at plume morphology and source separation.

While our method does not entirely eliminate false detections, it achieves a lower FP rate than basic thresholding methods by reducing background noise, which further reduces the need for manual inspection. Additionally, it has a lower computational cost than machine learning models as it needs no labeled training data or model training phase. Although initially developed to support the MethaneSAT mission, this plume detection framework is broadly applicable to a wide range of aircraft and satellite-borne platforms and use cases for emissions of methane and other species in both research and operational contexts.

https://doi.org/10.5194/egusphere-2026-141
Preprint. Discussion started: 30 January 2026

Code and data availability. MethaneAIR and MethaneSAT L3 concentration data can be accessed online from the Earth Engine Data Catalog at https://developers.google.com/earth-engine/datasets/tags/methanesat. The Python code of the wavelet method is available on GitHub: https://github.com/zhanzhangqq/wavelet_plume_finder_public.

Author contributions. ZZ, MS, AC, MR, and SA developed the methodology; ZZ, JDW, JPW, and KM analyzed the data; JB, MK, EK, CCM, SR, BL, DJM, MN, and KS produced input data; ZZ and MS wrote the manuscript draft; MO, LG, RG, JF, XL, and SCW reviewed and edited the manuscript.

Competing interests. The authors declare that they have no conflict of interest.

Acknowledgements. Funding for MethaneSAT and MethaneAIR activities was provided in part by an anonymous source, Arnold Ventures, The Audacious Project, Ballmer Group, Bezos Earth Fund, The Children's Investment Fund Foundation, Heising-Simons Family Fund, King Philanthropies, Robertson Foundation, Skyline Foundation, and Valhalla Foundation. For a more complete list of funders, please visit https://www.methanesat.org.

https://doi.org/10.5194/egusphere-2026-141
Preprint. Discussion started: 30 January 2026

References

Chan Miller, C., Roche, S., Wilzewski, J. S., Liu, X., Chance, K., Souri, A. H., Conway, E., Luo, B., Samra, J., Hawthorne, J., Sun, K., Staebell, C., Chulakadabba, A., Sargent, M., Benmergui, J. S., Franklin, J. E., Daube, B. C., Li, Y., Laughner, J. L., Baier, B. C., Gautam, R., Omara, M., and Wofsy, S. C.: Methane retrieval from MethaneAIR using the CO_2 proxy approach: a demonstration for the upcoming MethaneSAT mission, Atmospheric Measurement Techniques, 17, 5429–5454, https://doi.org/10.5194/amt-17-5429-2024, 2024.

Chulakadabba, A., Sargent, M., Lauvaux, T., Benmergui, J. S., Franklin, J. E., Chan Miller, C., Wilzewski, J. S., Roche, S., Conway, E., Souri, A. H., Sun, K., Luo, B., Hawthrone, J., Samra, J., Daube, B. C., Liu, X., Chance, K., Li, Y., Gautam, R., Omara, M., Rutherford, J. S., Sherwin, E. D., Brandt, A., and Wofsy, S. C.: Methane point source quantification using MethaneAIR: a new airborne imaging spectrometer, Atmospheric Measurement Techniques, 16, 5771–5785, https://doi.org/10.5194/amt-16-5771-2023, 2023.

Cusworth, D. H., Jacob, D. J., Varon, D. J., Chan Miller, C., Liu, X., Chance, K., Thorpe, A. K., Duren, R. M., Miller, C. E., Thompson, D. R., Frankenberg, C., Guanter, L., and Randles, C. A.: Potential of next-generation imaging spectrometers to detect and quantify methane point sources from space, Atmospheric Measurement Techniques, 12, 5655–5668, https://doi.org/10.5194/amt-12-5655-2019, 2019.

Duren, R., Cusworth, D., Ayasse, A., Howell, K., Diamond, A., Scarpelli, T., Kim, J., O'neill, K., Lai-Norling, J., Thorpe, A., Zandbergen, S. R., Shaw, L., Keremedjiev, M., Guido, J., Giuliano, P., Goldstein, M., Nallapu, R., Barentsen, G., Thompson, D. R., Roth, K., Jensen, D., Eastwood, M., Reuland, F., Adams, T., Brandt, A., Kort, E. A., Mason, J., and Green, R. O.: The Carbon Mapper emissions monitoring system, Atmospheric Measurement Techniques, 18, 6933–6958, https://doi.org/10.5194/amt-18-6933-2025, 2025.

Duren, R. M., Thorpe, A. K., Foster, K. T., Rafiq, T., Hopkins, F. M., Yadav, V., Bue, B. D., Thompson, D. R., Conley, S., Colombi, N. K., et al.: California's methane super-emitters, Nature, 575, 180–184, https://doi.org/10.1038/s41586-019-1720-3, 2019.

Ehret, T., De Truchis, A., Mazzolini, M., Morel, J.-M., D'aspremont, A., Lauvaux, T., Duren, R., Cusworth, D., and Facciolo, G.: Global tracking and quantification of oil and gas methane emissions from recurrent Sentinel-2 imagery, Environmental Science & Technology, 56, 10 517–10 529, https://doi.org/10.1021/acs.est.1c08575, 2022.

Guanter, L., Kaufmann, H., Segl, K., Foerster, S., Rogass, C., Chabrillat, S., Kuester, T., Hollstein, A., Rossner, G., Chlebek, C., Straif, C., Fischer, S., Schrader, S., Storch, T., Heiden, U., Mueller, A., Bachmann, M., Mühle, H., Müller, R., Habermeyer, M., Ohndorf, A., Hill, J., Buddenbaum, H., Hostert, P., Van der Linden, S., Leitão, P. J., Rabe, A., Doerffer, R., Krasemann, H., Xi, H., Mauser, W., Hank, T., Locherer, M., Rast, M., Staenz, K., and Sang, B.: The EnMAP spaceborne imaging spectroscopy mission for earth observation, Remote Sensing, 7, 8830–8857, https://doi.org/10.3390/rs70708830, 2015.

Guanter, L., Irakulis-Loitxate, I., Gorroño, J., Sánchez-García, E., Cusworth, D. H., Varon, D. J., Cogliati, S., and Colombo, R.: Mapping methane point emissions with the PRISMA spaceborne imaging spectrometer, Remote Sensing of Environment, 265, 112 671, https://doi.org/10.1016/j.rse.2021.112671, 2021.

Guanter, L., Roger, J., Warren, J., Sargent, M., Zhang, Z., Roche, S., Miller, C. C., Steiner, M., Hadfield, H., Omara, M., Williams, J. P., MacKay, K., Franklin, J. E., Wofsy, S. C., Hamburg, S. P., and Gautam, R.: Surveying Methane Point-Source Super-Emissions across Oil and Gas Basins with MethaneSAT, EGUsphere, 2025, 1–29, https://doi.org/10.5194/egusphere-2025-4666, 2025a.

Guanter, L., Warren, J., Omara, M., Chulakadabba, A., Roger, J., Sargent, M., Franklin, J. E., Wofsy, S. C., and Gautam, R.: Detection and quantification of methane plumes with the MethaneAIR airborne spectrometer, Atmospheric Measurement Techniques, 18, 3857–3872, https://doi.org/10.5194/amt-18-3857-2025, 2025b.

He, T.-L., Boyd, R. J., Varon, D. J., and Turner, A. J.: Increased methane emissions from oil and gas following the Soviet Union's collapse, Proceedings of the National Academy of Sciences, 121, e2314600 121, https://doi.org/10.1073/pnas.2314600121, 2024.

https://doi.org/10.5194/egusphere-2026-141
Preprint. Discussion started: 30 January 2026

Hüpfel, M., Kobitski, A. Y., Zhang, W., and Nienhaus, G. U.: Wavelet-based background and noise subtraction for fluorescence microscopy images, Biomedical Optics Express, 12, 969–980, https://doi.org/10.1364/BOE.413181, 2021.

Jacob, D. J., Turner, A. J., Maasakkers, J. D., Sheng, J., Sun, K., Liu, X., Chance, K., Aben, I., McKeever, J., and Frankenberg, C.: Satellite observations of atmospheric methane and their value for quantifying methane emissions, Atmospheric Chemistry and Physics, 16, 14 371–14 396, https://doi.org/10.5194/acp-16-14371-2016, 2016.

Jacob, D. J., Varon, D. J., Cusworth, D. H., Dennison, P. E., Frankenberg, C., Gautam, R., Guanter, L., Kelley, J., McKeever, J., Ott, L. E., Poulter, B., Qu, Z., Thorpe, A. K., Worden, J. R., and Duren, R. M.: Quantifying methane emissions from the global scale down to point sources using satellite observations of atmospheric methane, Atmospheric Chemistry and Physics, 22, 9617–9646, https://doi.org/10.5194/acp-22-9617-2022, 2022.

Jongaramrungruang, S., Thorpe, A. K., Matheou, G., and Frankenberg, C.: MethaNet — An AI-driven approach to quantifying methane point-source emission from high-resolution 2-D plume imagery, Remote Sensing of Environment, 269, 112 809, https://doi.org/10.1016/j.rse.2021.112809, 2022.

Radman, A., Mahdianpari, M., Varon, D. J., and Mohammadimanesh, F.: S2MetNet: A novel dataset and deep learning benchmark for methane point source quantification using Sentinel-2 satellite imagery, Remote Sensing of Environment, 295, 113 708, https://doi.org/10.1016/j.rse.2023.113708, 2023.

Rouet-Leduc, B. and Hulbert, C.: Automatic detection of methane emissions in multispectral satellite imagery using a vision transformer, Nature Communications, 15, 3801, https://doi.org/10.1038/s41467-024-47754-y, 2024.

Růžička, V., Mateo-Garcia, G., Gómez-Chova, L., Vaughan, A., Guanter, L., and Markham, A.: Semantic segmentation of methane plumes with hyperspectral machine learning models, Scientific Reports, 13, 19 999, https://doi.org/10.1038/s41598-023-44918-6, 2023.

Sánchez-García, E., Gorroño, J., Irakulis-Loitxate, I., Varon, D. J., and Guanter, L.: Mapping methane plumes at very high spatial resolution with the WorldView-3 satellite, Atmospheric Measurement Techniques, 15, 1657–1674, https://doi.org/10.5194/amt-15-1657-2022, 2022.

Scafutto, R. D. P. M. and De Souza Filho, C. R.: Detection of methane plumes using airborne midwave infrared (3–5 μm) hyperspectral data, Remote Sensing, 10, https://doi.org/10.3390/rs10081237, 2018.

Schneising, O., Buchwitz, M., Hachmeister, J., Vanselow, S., Reuter, M., Buschmann, M., Bovensmann, H., and Burrows, J. P.: Advances in retrieving XCH_4 and XCO from Sentinel-5 Precursor: improvements in the scientific TROPOMI/WFMD algorithm, Atmospheric Measurement Techniques, 16, 669–694, https://doi.org/10.5194/amt-16-669-2023, 2023.

Thompson, D. R., Leifer, I., Bovensmann, H., Eastwood, M., Fladeland, M., Frankenberg, C., Gerilowski, K., Green, R. O., Kratwurst, S., Krings, T., Luna, B., and Thorpe, A. K.: Real-time remote detection and measurement for airborne imaging spectroscopy: a case study with methane, Atmospheric Measurement Techniques, 8, 4383–4397, https://doi.org/10.5194/amt-8-4383-2015, 2015.

Thorpe, A. K., Green, R. O., Thompson, D. R., Brodrick, P. G., Chapman, J. W., Elder, C. D., Irakulis-Loitxate, I., Cusworth, D. H., Ayasse, A. K., Duren, R. M., Frankenberg, C., Guanter, L., Worden, J. R., Dennison, P. E., Roberts, D. A., Chadwick, K. D., Eastwood, M. L., Fahlen, J. E., and Miller, C. E.: Attribution of individual methane and carbon dioxide emission sources using EMIT observations from space, Science Advances, 9, eadh2391, https://doi.org/10.1126/sciadv.adh2391, 2023.

Varon, D. J., Jacob, D. J., McKeever, J., Jervis, D., Durak, B. O., Xia, Y., and Huang, Y.: Quantifying methane point sources from fine-scale satellite observations of atmospheric methane plumes, Atmospheric Measurement Techniques, 11, 5673–5686, https://doi.org/10.5194/amt-11-5673-2018, 2018.

Warren, J. D., Sargent, M., Williams, J. P., Omara, M., Miller, C. C., Roche, S., MacKay, K., Manninen, E., Chulakadabba, A., Himmelberger, A., Benmmergui, J., Zhang, Z., Guanter, L., Wofsy, S., and Gautam, R.: Sectoral contributions of high-emitting methane point sources

https://doi.org/10.5194/egusphere-2026-141
Preprint. Discussion started: 30 January 2026

from major U.S. onshore oil and gas producing basins using airborne measurements from MethaneAIR, Atmospheric Chemistry and Physics, 25, 10 661–10 675, https://doi.org/10.5194/acp-25-10661-2025, 2025.

Williams, J. P., Benmergui, J., Knapp, M., Omara, M., Himmelberger, A., Kyzivat, E., Weatherby, K., Lyke, B., Warren, J., MacKay, K., Ayvazov, S., Russi, M., LoFaso, N., Melendez, T., Miller, C. C., Roche, S., Sargent, M., Franklin, J., Nasr, M., Zhang, Z., Miller, D., Luo, B., Guanter, L., Hamburg, S. P., Wofsy, S. C., and Gautam, R.: Methane intensity and emissions across major oil and gas basins and individual jurisdictions using MethaneSAT observations, EGUsphere, 2025, 1–30, https://doi.org/10.5194/egusphere-2025-6126, 2025.

Xiao, C., Fu, B., Shui, H., Guo, Z., and Zhu, J.: Detecting the sources of methane emission from oil shale mining and processing using airborne hyperspectral data, Remote Sensing, 12, https://doi.org/10.3390/rs12030537, 2020.